Research Article Vol. 63, No. 13 / 1 May 2024 / Applied Optics 3445

applied optics

Temperature effects in narrow-linewidth optical cavity control with a surrogate quasi-second-harmonic field

Li-Wei Wei,[1,2,*] Jan Hendrik Põld,[1] Dennis Schmelzer,[1] Kanioar Karan,[1] and Benno Willke[1]

[1]Institut für Gravitationsphysik der Leibniz Universität Hannover and Max Planck Institute for Gravitational Physics (Albert Einstein Institute), Callinstraße 38, 30167 Hannover, Germany
[2]Deutsches Elektronen-Synchrotron DESY, Notkestr. 85, 22607 Hamburg, Germany
*li-wei.wei@desy.de

Received 24 January 2024; revised 2 April 2024; accepted 2 April 2024; posted 3 April 2024; published 24 April 2024

Fabry–Perot cavities are widely used in precision interferometric applications. Various techniques have been developed to achieve the resonance condition via the direct interrogation of the cavity with the main laser field of interest. Some use cases, however, require a surrogate field for cavity control. In this study, we construct a bichromatic cavity to study the surrogate control approach, where the main and the surrogate fields are related by the second-harmonic generation with nonlinear optics. We experimentally verify the temperature dependence of the differential reflection phase of a dielectric coating design optimized for the surrogate control approach of the optical cavities of the light-shining-through-a-wall experiment Any Light Particle Search II and develop a comprehensive cavity model for quasi-second-harmonic resonances that considers also other important factors, such as the Gouy phase shift, for a detailed analysis of the surrogate control approach.

https://doi.org/10.1364/AO.519988

1. INTRODUCTION

Fabry–Perot cavities find many use cases in precision interferometry and are at the forefront of several fundamental scientific explorations. An outstanding instance are the laser interferometric gravitational wave detectors, in which Fabry–Perot cavities are exploited for their intracavity power buildup, spatial-mode selectivity, noise filtering property, and/or signal enhancement property [1–3].

In most cases, the resonance condition between the continuous-wave laser field of interest and the optical cavity is achieved via their direct interaction. Some form of error signal is generated for the control loop that actuates on either the optical frequency of the laser field or the length of the optical cavity. The error signal can be based on the transmission/reflection fringes, the introduction of modulation sidebands and heterodyne techniques [4,5], polarization spectroscopy [6], and spatial mode interference [7].

For the first observation of gravitational waves from a binary black hole merger [8], the Laser Interferometer Gravitational-Wave Observatory (LIGO) achieved a strain sensitivity of better than $10^{-23}/\sqrt{\text{Hz}}$ at around 100 Hz [9]. Further improvements to the strain sensitivity of gravitational wave detectors are planned, and one of the promising techniques is the injection of frequency-dependent squeezed vacuum state of light into the detector [10]. Typically, this involves first the generation of squeezed vacuum states whose squeeze angle is frequency-independent. A detuned (from exact resonance with the laser field) optical cavity is then used to generate the frequency-dependent rotation of the squeeze angle [11,12].

Since there is no coherent amplitude associated with the squeezed vacuum state, a surrogate field is required to achieve the resonance condition, with controlled detuning, between the squeezed vacuum state and the optical cavity. A quasi-second-harmonic field is currently used for such a surrogate task to generate the frequency-dependent squeezed vacuum state for the advanced gravitational-wave detectors [13–15].

High-finesse Fabry–Perot cavities can also be exploited to resonantly enhance the sensitivity of light-shining-through-a-wall experiments [16–18] searching for ultralight bosonic dark matter candidate particles such as the axion and the axion-like particles (ALPs) [19–22], as illustrated in Fig. 1.

In a light-shining-through-a-wall experiment, the hypothetical ALPs are produced via their interaction with photons in the presence of a magnetic field. Conversely, ALPs can also regenerate into photons in the presence of a magnetic field. Enclosing the ALPs' production and the photon regeneration

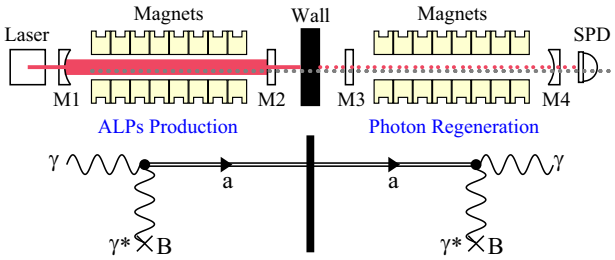

Fig. 1. Schematic of a dual optical cavity enhanced light-shining-through-a-wall experiment and its Feynman diagram representation, where γ denotes a photon, a denotes the axion-like particles (ALPs) and B denotes the magnetic field. M: Mirror; M1 and M2 form the (axion-) production cavity, and M3 and M4 form the (photon-) regeneration cavity; SPD: single-photon detector; solid red lines, input and circulating laser beams; gray dotted line, axion-like particles; red dotted line, regenerated photons.

areas with optical cavities increases the probability of a laser photon reaching the single-photon detector (Fig. 1).

With a symmetric lossless optical cavity, the probability is increased by a gain factor of $1/\mathcal{T}$, where $\mathcal{T}$ is the transmissivity of the cavity mirrors [23]. The Any Light Particle Search II (ALPS II) experiment will be the first dual optical cavity enhanced light-shining-through-a-wall experiment, and anticipates a combined signal enhancement factor of 2×10^8 from two optical cavities [24].

The projected signal power on the single-photon detector at the targeted search sensitivity of the ALPS II experiment is of the order of two photons per day. This can be detected with a transition edge sensor, which is a calorimeter that operates at cryogenic temperatures capable of detecting single-photon energies on the order of ≈ 1 eV, and has been shown to exhibit an intrinsic background rate as low as 6.9×10^{-6} Hz [25,26].

The feeble signal power also poses challenges in controlling the optical cavity. The shot noise of a sensible laser beam that is used to interrogate the cavity will overwhelm the feeble signal. A quasi-second-harmonic surrogate field for optical cavity control is therefore also planned for the ALPS II experiment [24]. Dichroic optics can then be used to attenuate the surrogate field, or ideally, to prevent the surrogate field from reaching the transition edge sensor. In practice, any residual surrogate field that reaches the transition edge sensor can also be vetoed by the calorimetric difference between the fundamental signal field and the quasi-second-harmonic surrogate field. For instance, the transition edge sensor being developed for ALPS II has achieved an energy resolution of around 11% [26].

In general, there exists a temperature dependence of the differential reflection phase between the fundamental and the quasi-second-harmonic fields of the dielectric coatings that constitute the optical cavity. Uncontrolled temperature in conjunction with such temperature dependence can harm the fidelity of the surrogate cavity control scheme [27]. In this paper, we present our work on the experimental verification of the temperature optimized dielectric coating design proposed in [27]. In addition, to better understand the results of our experiment, we construct a comprehensive model that considers also the effect of the length and the geometry of the optical cavity on its control with a surrogate quasi-second-harmonic field.

2. SURROGATE OPTICAL CAVITY CONTROL

Figure 2 shows a generic schematic for surrogate optical cavity control. The relation in optical frequency ν between Laser 1 and Laser 2 is maintained by a phase-locked loop (PLL). Laser 2 is frequency-doubled by a second-harmonic generation unit and injected to the bichromatic cavity that consists of mirrors M1 and M2 at a distance L apart. The resonance condition between Laser 2 and the cavity can be maintained using, e.g., the Pound–Drever–Hall (PDH) technique [4,5]. A frequency offset in the PLL is generally required to account for dispersive effects. This is to account for the fact that bichromatic cavity resonance is generally not possible for exact harmonic fields, as we will see in the following.

One dispersive effect is the reflection phase of dielectric coatings, which would require, to first order, a frequency offset of [27]

$$f = \frac{c}{2L} \cdot \frac{1}{2\pi} \cdot 2 \cdot \phi_{\text{diff}}, \tag{1}$$

where

$$\phi_{\text{diff}} \equiv \frac{\phi(\nu_2)}{2} - \phi(\nu_1), \tag{2}$$

denote the difference in the reflection phase between the fundamental field ν_1 and its quasi-second-harmonic field ν_2.

In the surrogate control scheme, a frequency offset f for bichromatic cavity resonance is not an issue by itself. The important requirement is that f remains constant such that ν_1 is always resonant with the bichromatic cavity as long as the frequency-offset PLL between Laser 1 and Laser 2, and the PDH control loop between Laser 2 and the bichromatic cavity are in operation.

In the presence of temperature fluctuations ΔT, the offset frequency f will change by

$$\Delta f = \frac{c}{2L} \cdot \frac{1}{2\pi} \cdot 2 \cdot \frac{\mathrm{d}\phi_{\text{diff}}}{\mathrm{d}T} \cdot \Delta T. \tag{3}$$

To maintain a constant offset frequency f for bichromatic cavity resonance, the temperature dependence of the coating reflection phase of the quasi-second-harmonic field needs to be twice that of the fundamental field.

In the ALPS II experiment, optical cavities of ≈ 120 m baseline have been set up [28], and target at finesse values of up to

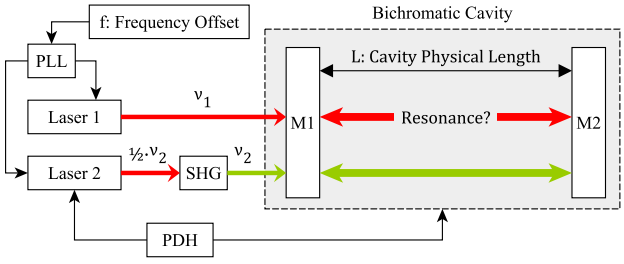

Fig. 2. The bichromatic cavity and the surrogate control scheme. The resonance condition between ν_1 and the bichromatic cavity depends on the resonance condition between ν_2 and the bichromatic cavity, as well as the frequency offset of the phase-locked loop between ν_1 and ν_2. M: mirror; SHG: second-harmonic generation; PLL: phase-locked loop; PDH: the Pound–Drever–Hall sensing and control technique.

120,000 [24]. The combination results effectively in a cavity linewidth as narrow as ≈ 10 Hz, and therefore enforces strict control requirements on Δf.

Equation (3) indicates that Δf can be contained by having a stable temperature and/or a coating with minimized $\mathrm{d}\phi_{\mathrm{diff}}/\mathrm{d}T$. The latter can be achieved by using different bilayers to construct the coating as presented in [27]. One of the main goals of this study is to experimentally verify such coating design concept.

3. EXPERIMENTAL SETUP AND MEASUREMENT DATA

In this study, we construct a plano–concave bichromatic optical cavity to experimentally examine the surrogate control scheme. The experimental setup is shown in Fig. 3. One-inch (25.4 mm) optics are used for our experiment.

The concave mirror of the bichromatic cavity has a radius of curvature of 2 m. The planar and the concave mirrors are attached to an aluminum spacer with a nominal length of 0.2715 m. Both cavity mirrors are coated with seven multiband reflector (MBR) bilayers on top of 11 quarter-wave stack (QWS) bilayers, and capped with a customary half-wave layer (HW) at ν_1; the dual-band reflector stack has a center wavelength at optical frequency $(\nu_1 + \nu_2)/2$, and the quarter-wave stack has a center wavelength at optical frequency ν_1 [27]. Silica (SiO_2) is used as the low-index coating material and tantala (Ta_2O_5) is used as the high-index coating material. The mirror substrate material is silica. The coating design is illustrated in Fig. 4.

The refractive indices of the coating materials from the vendor of the coating are used to simulate the nominal characteristics of the cavity mirror coating and its sensitivity to manufacture tolerances with Monte Carlo methods. The results with 1000 trials are shown in Fig. 5 and summarized in Table 1.

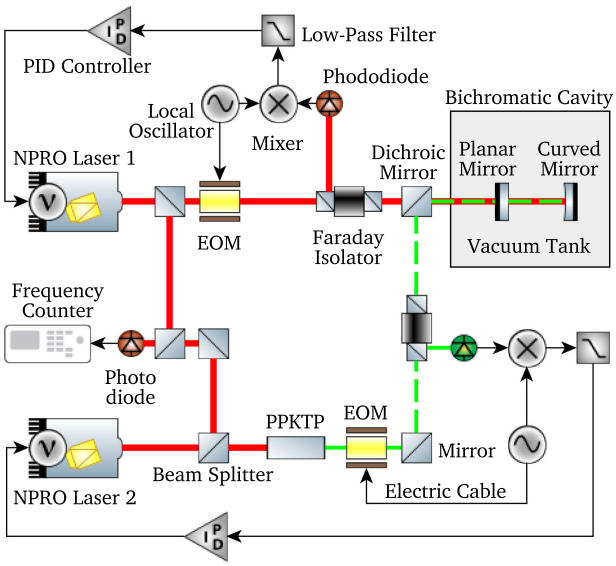

Fig. 3. Schematic of the experimental setup. Mode-matching optics are not shown for conciseness. NPRO, nonplanar ring oscillator; EOM: electro-optical modulator; PPKTP: periodically poled potassium titanyl phosphate ($KTiOPO_4$); PID, proportional–integral–derivative.

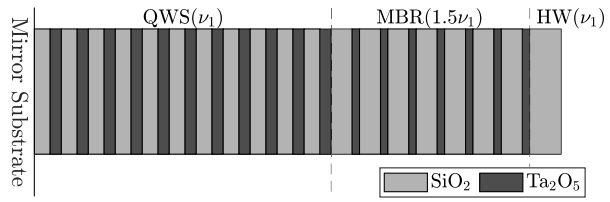

Fig. 4. Dielectric coating for the bichromatic cavity mirrors in this study. The mirror substrate material is silica. QWS, quarter-wave stack; MBR, multiband reflector; HW, half-wave.

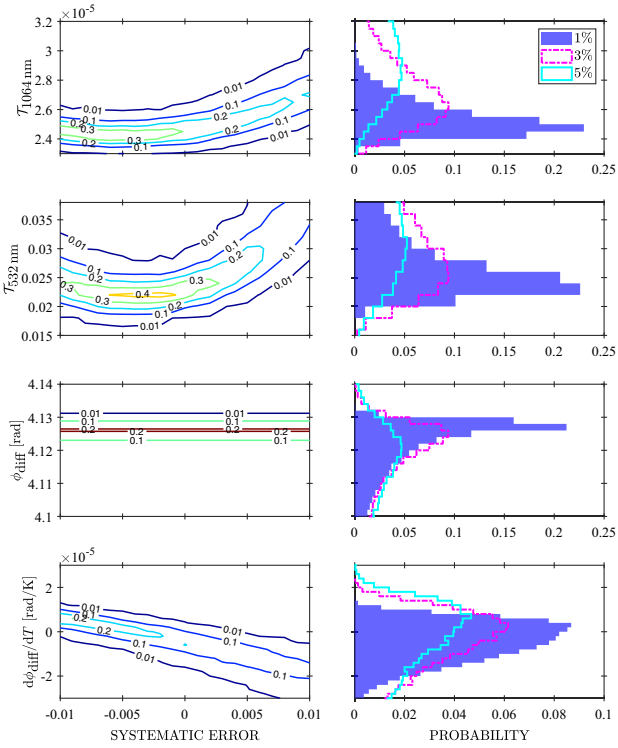

Fig. 5. Distributions of the coating parameters extracted from Monte Carlo simulations in the presence of systematic and random errors in layer thickness: $\mathcal{T}_{1064\,\mathrm{nm}}$ and $\mathcal{T}_{532\,\mathrm{nm}}$ are the transmissivity values at 1064 and 532 nm wavelengths, respectively; ϕ_{diff} and $\mathrm{d}\phi_{\mathrm{diff}}/\mathrm{d}T$ are the difference in reflection phase [Eq. (2)] and its temperature dependence. On the left panel, the x axis is the systematic error, the y axis is the parameters of interest, and the contour denotes the probability value of the normalized histograms of the Monte Carlo results at each systematic error value; normally distributed random errors with 1% standard deviation are used in the left panel. The data with different systematic errors are then combined to produce the accumulated histograms in the right panel; the systematic error is assumed to be uniformly distributed. Data using random errors with 3% and 5% standard deviation are additionally plotted in the right panel. The bin widths for $\mathcal{T}_{1064\,\mathrm{nm}}$, $\mathcal{T}_{532\,\mathrm{nm}}$, ϕ_{diff}, and $\mathrm{d}\phi_{\mathrm{diff}}/\mathrm{d}T$ are 0.5 ppm, 0.2%, 2 mrad, and 2 µrad/K, respectively. We note that in order to have a clearer illustration on the distribution of the parameters within the requirements, the histograms are clipped.

More details on the Monte Carlo simulations can be found in [27].

Two NPRO lasers [29] at ≈ 1064 nm wavelength are used to provide light with optical frequencies ν_1 and $\nu_2/2$ and to adjust the frequency offset $f = \nu_2/2 - \nu_1$. NPRO 2 is sent to

Table 1. Summary of the Simulated Characteristics of the Bichromatic Cavity Mirror Coating Shown in Fig. 5[a]

	ν_1	ν_2
Wavelength	1064 nm	532 nm
$\mathcal{T}$	$24.7^{+3.0}_{-1.8}$ppm	$2.34^{+1.71}_{-0.62}$%
ϕ_{diff}	$4.1251^{+0.0085}_{-0.0246}$rad	
$\mathrm{d}\phi_{\text{diff}}/\mathrm{d}T$	$(-0.342 \pm 1.709) \times 10^{-5}$ rad/K	

[a]The uncertainty range corresponds to 95% inclusion of the Monte Carlo data points with random errors of 1% standard deviation. The uncertainty range is derived symmetrically about the nominal values and capped with the maximum/minimum values of the simulated data set.

a periodically poled $KTiOPO_4$ (PPKTP) crystal for its second-harmonic generation to ≈ 532 nm wavelength. The PPKTP crystal is temperature-stabilized for optimal phase matching and conversion efficiency.

The optical frequencies of NPRO 1 and NPRO 2 are stabilized to the length of the test cavity with the PDH technique [4,5], at ≈ 1064 nm (ν_1) and ≈ 532 nm (ν_2) wavelengths, respectively. NPRO 1 and the fundamental field of NPRO 2 are spatially overlapped to generate an interference beat note focused on a fast photodiode.

A heating foil, a thermistor, and two thermocouples are attached to the cavity spacer. The test cavity is mounted on an optical breadboard and placed in a vacuum tank. Insulating elastomer supports are used in between the breadboard and the base plate of the vacuum tank. The thermal time constant of the entire in-vacuum assembly is measured to be ≈ 5.56 h. The flexibility of the elastomer allows the cavity spacer and the optical breadboard, both made of aluminum, to expand and contract with minimal constraints, thereby reducing thermally induced deformation other than length changes. The cavity mirrors are spring-loaded to the cavity spacer to minimize the deformation of the mirrors under temperature changes. The vacuum tank is mounted on the optical table where all other optical components are placed.

The cavity spacer is heated to various temperatures with the heating foil. Upon reaching thermal equilibrium, the two NPRO lasers are frequency-stabilized to the length of the bichromatic cavity, and the difference in their optical frequencies is measured with a frequency counter of 350 MHz bandwidth.

Taking into account the coating reflection phase $\phi(\nu_i)$, the resonant optical frequencies for a linear cavity with identical mirror coatings are, in plane-wave formulation,

$$\nu_i = \frac{c}{2L} \cdot \left[N_i + \frac{2 \cdot \phi(\nu_i)}{2\pi} \right], \tag{4}$$

where N is an integer and i denotes the fundamental field ($i = 1$) and the quasi-second-harmonic ($i = 2$) field. The frequency offset f required for surrogate cavity control is

$$f = \frac{\nu_2}{2} - \nu_1 = \frac{c}{2L} \left[\frac{N_2}{2} - N_1 + \frac{1}{2} \cdot \frac{2 \cdot \phi(\nu_2)}{2\pi} - \frac{2 \cdot \phi(\nu_1)}{2\pi} \right]. \tag{5}$$

Equation (5) reiterates that a nonzero offset frequency f is generally required for surrogate cavity control with a harmonic field. Furthermore, as a consequence of the frequency-doubling process (i.e., $\nu_2 \approx 2 \cdot \nu_1$), when the optical frequencies of NPRO 1 and NPRO 2 are scanned simultaneously, we will see two resonances of ν_2 per each free spectral range (FSR) of ν_1 (see Fig. 6). This also means that every time N_1 increases by 1 in Eq. (5), N_2 needs to increase by 2 to result in roughly the same offset frequency f.

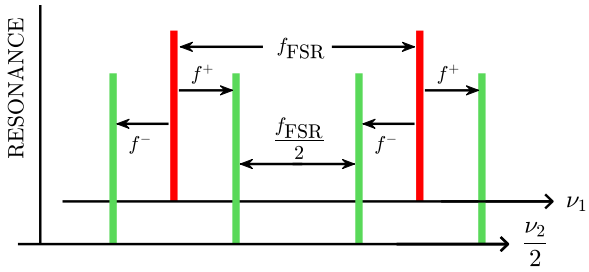

Fig. 6. Relation between the resonant optical frequencies of the bichromatic cavity.

Similarly, with the increment or decrement of 1 in N_2, the offset frequency f can either become positive or negative. The sign of the beat note frequency cannot be determined by the frequency counter, and is instead calibrated to the PZT and temperature tuning coefficients of the NPRO laser crystals. We refer to the positive and the negative frequency offsets with the least absolute values as f^+ and f^-, respectively.

The change in f with an increment of 1 in N_1 or an increment of 2 in N_2 corresponds to the cavity FSR and allows for a direct frequency-based measurement of the cavity FSR. The FSR of our 0.2715 m long cavity is $f \approx 552.1$ MHz and therefore exceeds the detection bandwidth of 350 MHz of the frequency counter in our setup. A change in f with an increment of 1 in N_2 corresponds to one-half of the cavity FSR, which is then measurable by our frequency counter. In practice, this is done via the measurements on f^+, f^-, and the relation

$$f_{\text{FSR}} \equiv c/(2L) = 2 \cdot (f^+ - f^-). \tag{6}$$

The resonant optical frequencies ν_1, ν_2 of the bichromatic cavity are illustrated in Fig. 6. The measured f^+, f^-, and the derived f_{FSR} at various temperatures of our test cavity setup are shown in Fig. 7.

4. DATA ANALYSIS AND PARAMETER EXTRACTION

For quasi-harmonic fields, $N_2 = 2 \cdot N_1$, and Eq. (5) can be simplified to

$$f \approx \frac{c}{2L} \cdot \frac{1}{2\pi} \cdot \left[\phi(\nu_2) - 2 \cdot \phi(\nu_1) \right] \equiv \frac{c}{2L} \cdot \frac{1}{2\pi} \cdot 2 \cdot \phi_{\text{diff}}. \tag{7}$$

Taking the derivative of Eq. (7) with respect to T, we have

$$\frac{\mathrm{d}f}{\mathrm{d}T} = -\frac{c}{2L^2} \frac{\mathrm{d}L}{\mathrm{d}T} \frac{2 \cdot \phi_{\text{diff}}}{2\pi} + \frac{c}{2L} \frac{1}{2\pi} \frac{2 \cdot \mathrm{d}\phi_{\text{diff}}}{\mathrm{d}T}, \tag{8}$$

$$= -f \cdot \alpha_{\text{CTE}} + \frac{c}{2L} \frac{1}{\pi} \frac{\mathrm{d}\phi_{\text{diff}}}{\mathrm{d}T}. \tag{9}$$

The temperature dependence measurements of f therefore contain information on $\mathrm{d}\phi_{\text{diff}}/\mathrm{d}T$.

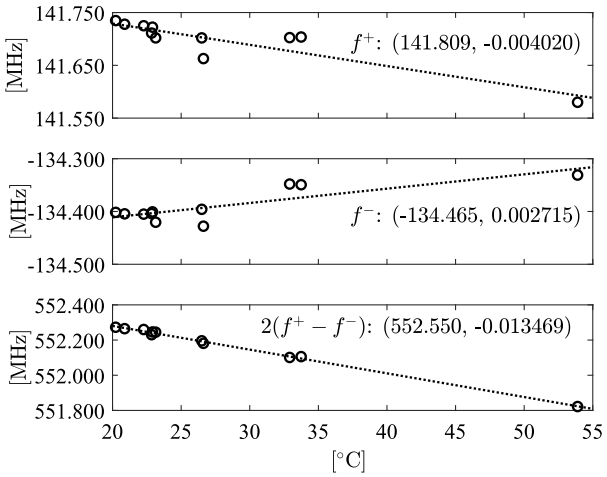

Fig. 7. Temperature dependence measurements (circle) of f^+, f^-, and f_{FSR}, with linear fits $y = a + bx$ (dotted line) denoted as (a, b). The rmses of the linear fits are 20.1 kHz for f^+, 18.7 kHz for f^-, and 8.2 kHz for $2(f^+ - f^-)$.

In our setup, the length of the test cavity L is not held constant with a stabilization scheme. As the setup is heated, the cavity elongates, resulting in a decrease in FSR. The expected slope can be derived by

$$\frac{\mathrm{d}f_{\mathrm{FSR}}}{\mathrm{d}L}\frac{\mathrm{d}L}{\mathrm{d}T} = -\frac{c}{2L^2}\cdot L\cdot\alpha_{\mathrm{CTE}} = -\frac{c}{2L}\cdot\alpha_{\mathrm{CTE}}, \tag{10}$$

where α_{CTE} is the coefficient of thermal expansion. The slope of the linear fit of our measurement (see Fig. 7, bottom subplot) on f_{FSR} is ≈ -13.5 kHz/K, which for our 0.2715 m long bichromatic optical cavity projects to an α_{CTE} of 24.5 ppm/K, which is slightly higher than the typical value of 24 ppm/K for aluminum [30]. The discrepancy is likely in part due to errors in our temperature measurements based on an NTC 10 K thermistor, which has a typical uncertainty of ±1%. The root-mean-square error (rmse) of the linear fit is 8.2 kHz.

The value of the first term in Eq. (9) can be derived from the measured f^+, f^-. Using $f^+ \approx 141.7$ MHz and $f^- \approx -134.4$ MHz, we have

$$-f^+\cdot\alpha_{\mathrm{CTE}} \approx -3.46\ \mathrm{kHz/K}, \tag{11}$$

$$-f^-\cdot\alpha_{\mathrm{CTE}} \approx +3.29\ \mathrm{kHz/K}. \tag{12}$$

The net slopes after removing the effect from cavity elongation are

$$\frac{\mathrm{d}f^+}{\mathrm{d}T} + f^+\cdot\alpha_{\mathrm{CTE}} \approx -0.55\ \mathrm{kHz/K}, \tag{13}$$

$$\frac{\mathrm{d}f^-}{\mathrm{d}T} + f^-\cdot\alpha_{\mathrm{CTE}} \approx -0.57\ \mathrm{kHz/K}. \tag{14}$$

The second term in Eq. (9) does not depend on the offset frequency, so an ideal measurement should result in the same net slope from f^+ and f^-. Our measurement results can be combined into

$$\frac{c}{2L}\frac{1}{\pi}\frac{\mathrm{d}\phi_{\mathrm{diff}}}{\mathrm{d}T} \approx (-0.56\pm0.01)\ \mathrm{kHz/K}, \tag{15}$$

which corresponds to

$$\frac{\mathrm{d}\phi_{\mathrm{diff}}}{\mathrm{d}T} \approx (-3.20\pm0.05)\ \mu\mathrm{rad/K}. \tag{16}$$

The measured temperature dependence in differential reflection phase of the bichromatic cavity mirror coatings matches closely the nominal value given in Table 1. This not only verifies the coating design concept in [27] but also indicates that the manufacture errors are well contained during the coating process.

A temperature dependence in differential reflection phase of around 114 Hz/K was reported for the 285 m long Advanced Virgo filter cavity [15]. If we assume identical contribution from the two cavity mirrors, in analogy to Eq. (15), we have

$$\frac{c}{2\cdot 285\ \mathrm{m}}\frac{1}{\pi}\frac{\mathrm{d}\phi_{\mathrm{diff}}}{\mathrm{d}T} \approx 114\ \mathrm{Hz/K}, \tag{17}$$

$$\frac{\mathrm{d}\phi_{\mathrm{diff}}}{\mathrm{d}T} \approx 681\ \mu\mathrm{rad/K}. \tag{18}$$

Our optimized bichromatic dielectric coating design exhibits a reduction of over factor 200 in comparison.

5. EXTENDED MODEL FOR IMPROVED DATA ANALYSIS

As can be seen in Fig. 7, in comparison to the measurement of f_{FSR}, the departure of the measured data points of f^+ and f^- from their respective linear fits is more pronounced. The rmse is 20.1 kHz for f^+ and 18.7 kHz for f^-. Additionally, the measured offset frequencies f^+ and f^- cannot be correctly calculated from Eq. (7) with the parameters specified in Table 1.

This prompts further generalization in modeling the bichromatic optical cavity, for which we consider the inclusion of the Gouy phase shift ψ that is characteristic to Gaussian beams, and elevate the length of the cavity to be a variable that can also be different for the two wavelengths. In our definition, the cavity length is the effective distance between the surfaces of the mirrors as seen by the Gaussian beams, which could be different for the two wavelengths due to the different sampled areas on the mirror surfaces. Equation (4) is thus expanded to

$$\begin{aligned}\nu_i &= \frac{c}{2L(\nu_i)}\cdot\left[N_i + \frac{2\cdot\phi(\nu_i)}{2\pi} + \frac{2\cdot\psi(\nu_i)}{2\pi}\right]\\ &\equiv \frac{c}{2(L+M_i)}\left[N_i + 2\Phi_i + 2\Psi_i\right],\end{aligned} \tag{19}$$

where, for conciseness, we have introduced the following: $L(\nu_i) \equiv L + M_i$, $\Phi_i = \phi(\nu_i)/(2\pi)$, $\Psi_i = \psi(\nu_i)/(2\pi)$. Consequently, the offset frequency f becomes

$$\begin{aligned}f = \frac{\nu_2}{2} - \nu_1 &= \frac{c}{2(L+M_2)}\frac{(N_2 + 2\Phi_2 + 2\Psi_2)}{2}\\ &- \frac{c}{2(L+M_1)}\left(N_1 + 2\Phi_1 + 2\Psi_1\right).\end{aligned} \tag{20}$$

We introduce

$$N_{\mathrm{diff}} \equiv N_2 - 2N_1, \quad \Phi_{\mathrm{diff}} \equiv \frac{\Phi_2}{2} - \Phi_1, \quad \Psi_{\mathrm{diff}} \equiv \frac{\Psi_2}{2} - \Psi_1, \tag{21}$$

and

$$\epsilon_i \equiv \frac{M_i}{L} \ll 1, \quad \epsilon_{\mathrm{diff}} = \frac{M_2 - M_1}{L} \ll 1, \tag{22}$$

to recast Eq. (20) into the approximation

$$f \approx \frac{c}{2L}\left[\frac{N_{\mathrm{diff}}}{2} + 2\cdot\Phi_{\mathrm{diff}} + 2\cdot\Psi_{\mathrm{diff}} - \epsilon_{\mathrm{diff}}\cdot N_1\right]. \tag{23}$$

A. Gouy Phase Shift and the Frequency Offset

The first two terms in the square brackets of Eq. (23) have already been discussed so far. The second term Φ_{diff} is readily available from Table 1,

$$\Phi_{\mathrm{diff}} = \frac{\phi_{\mathrm{diff}}}{2\pi} \approx 0.656530^{+0.001353}_{-0.003915}. \tag{24}$$

The third term accounts for the Gouy phase shift $\psi = z/z_R$ of a fundamental Gaussian beam with Rayleigh range z_R at a distance z from the beam waist. The Rayleigh range z_R and the distance z also determine the radius of curvature of the wavefront, which needs to match those of the cavity mirrors. The z_R of the resonant Gaussian beam is therefore determined by the geometry of the optical cavity and is in principle wavelength-independent. This means that we can generally take the assumption that $\Psi_1 \approx \Psi_2$, and this leads to

$$\Psi_{\mathrm{diff}} \approx -\frac{\Psi_1}{2} \approx -\frac{\Psi_2}{2}. \tag{25}$$

For our plano–convex cavity with length $L = 0.2715$ m and curved mirror radius of curvature $R = 2$ m, we have

$$\Psi_1 \approx \Psi_2 \approx \frac{1}{2\pi}\cdot \mathrm{acos}\left(\sqrt{1 - \frac{L}{R}}\right) \approx 0.060054. \tag{26}$$

Neglecting the fourth term of Eq. (23), the nominal frequency offsets f for $N_{\mathrm{diff}} = 0 \ldots -4$ are summarized in Table 2.

The two f's that fall into our detection bandwidth match well with the measured f^+ and f^- shown in Fig. 7; the difference is around 2.0 MHz for both f^+ and f^-. Using Eq. (23), the uncertainty on ϕ_{diff} in Table 1 corresponds to an uncertainty range of around [−4.3 MHz, +1.5 MHz] on f. The measured f's are therefore slightly outside the uncertainty range given by the coating simulations.

Table 2. Nominal and Measured Frequency Offsets for our Bichromatic Optical Cavity at Room Temperature

N_{diff}	f_{nominal}	Remark
0	+691.79 MHz	
−1	+415.74 MHz	
−2	+139.68 MHz	$f^+_{\mathrm{measured}} \approx 141.7$ MHz
−3	−136.37 MHz	$f^-_{\mathrm{measured}} \approx -134.4$ MHz
−4	−412.42 MHz	

B. Differential Cavity Lengths and Mirror Radius of Curvature

The term that contains ϵ_{diff} in Eq. (23) can be rewritten as

$$f_\epsilon \equiv -\frac{c}{2L}\cdot\epsilon_{\mathrm{diff}}\cdot N_1 = -\nu_1\cdot\epsilon_{\mathrm{diff}}, \quad \frac{f_\epsilon}{\nu_1} \equiv -\epsilon_{\mathrm{diff}}, \tag{27}$$

which resembles the perturbative cavity resonance condition of

$$\frac{\delta\nu}{\nu} = -\frac{\delta L}{L}. \tag{28}$$

This indicates that, to result in a change of f of ≈ 2 MHz, a ≈ 2 nm difference between M_1 and M_2 is required. For the excess of about 0.5 MHz discussed above, a ≈ 0.5 nm difference between M_1 and M_2 is required, which is within the range reported in [31].

We note that in the case of $M_1 \neq M_2$, the thermal elongation of the cavity also causes the frequent offset f to change by

$$\frac{\partial f}{\partial L}\frac{\partial L}{\partial T} = \nu_1\cdot\epsilon_{\mathrm{diff}}\cdot\alpha_{\mathrm{CTE}}, \tag{29}$$

which is on the order of 25 Hz/K per nanometer difference between M_1 and M_2 for our bichromatic cavity.

Changes in the cavity length can also lead to changes in the Gouy phase shift, and in turn lead to changes in the frequency offset. For a plano–concave cavity, it can be shown that

$$\frac{\mathrm{d}\psi}{\mathrm{d}L} = \frac{1}{2\sqrt{L\cdot(R-L)}} = \frac{1}{2z_R}, \tag{30}$$

The Rayleigh range z_R of our bichromatic optical cavity is ≈ 0.685 m. As this is a second-order effect, a 2 nm change in L corresponds to a negligible change of 0.128 Hz in f.

Changes in the radius of curvature of the curved mirror also lead to changes in the frequency offset as

$$\frac{\mathrm{d}\psi}{\mathrm{d}R} = -\frac{1}{2z_R}\cdot\frac{L}{R}. \tag{31}$$

A change of ≈ 2 MHz in the frequency offset requires a common mode $\delta R/R$ of ≈ 11.5%. The higher-order mode spacing of our bichromatic cavity is measured to be (66.50 ± 0.07) MHz at 1064 nm, which corresponds to a one-way Gouy phase shift of $\Psi \approx 0.060226 \pm 0.000063$, which matches the value in Eq. (26) to within 0.3%. Assuming the other mirror to be perfectly planar, the corresponding radius of curvature of the curved mirror is $R \approx (1.989 \pm 0.004)$ m.

It is possible that the radius of curvature sensed by the two quasi-harmonic wavelengths differ from each other, as the beam spot radius on the curved mirror is different for the two wavelengths. We have only measured the radius of curvature with the fundamental field and therefore cannot draw any conclusions on this.

C. Gouy Phase Shift and the Temperature Dependence of the Frequency Offset

In Section 4, we have derived the temperature dependence in differential reflection phase result of our experiment [Eq. (16)] in plane-wave formulation.

For Gaussian beams, as Eq. (23) indicates, temperature-induced changes in the Gouy phase shift also contributes to the temperature dependence of f. For our bichromatic cavity, considering also Eqs. (25) and (30), the contribution of the Gouy phase shift term due to temperature-induced cavity length change can be derived as

$$\begin{aligned}\frac{\partial f}{\partial \Psi_{\text{diff}}}\frac{\partial \Psi_{\text{diff}}}{\partial L}\frac{\partial L}{\partial T} &= -\frac{1}{2}\frac{\partial f}{\partial \Psi_{\text{diff}}}\frac{\partial \Psi_1}{\partial L}\frac{\partial L}{\partial T}\\ &= -\frac{1}{2}\cdot\frac{c}{L}\cdot\frac{1}{2z_R\cdot 2\pi}\cdot L\cdot\alpha_{\text{CTE}}\\ &= -\frac{c}{8\pi z_R}\cdot\alpha_{\text{CTE}}\\ &\approx -0.43\,\text{kHz/K}, \end{aligned} \tag{32}$$

which should be accounted for in deriving Eqs. (15) and (16).

After correcting for the contribution of the Gouy phase shift term derived in Eq. (32), the measured temperature dependence in differential reflection phase of the bichromatic cavity mirror coatings further reduces in terms of absolute value to

$$\frac{\mathrm{d}\phi_{\text{diff}}}{\mathrm{d}T} \approx (-0.75 \pm 0.05)\ \mu\text{rad/K}. \tag{33}$$

On the other hand, we have to note that the contribution of the Gouy phase shift term due to temperature-induced change in mirror radius of curvature may also be considered when the mirror is confined. In our bichromatic cavity, the mirrors are spring-loaded and therefore we do not consider such an effect.

D. Wavelength Dependence

Equations (20) and (23) indicate that, in the case of $M_1 \neq M_2$, when N_1 takes an increment of 1, even with an increment of 2 on N_2, the frequency offset f is slightly perturbed. In other words, the frequency offset f depends on the absolute optical frequencies of the lasers.

Even in the case of $M_1 = M_2$, the wavelength dependence of coating reflection phase leads to a similar effect. To show this, we expand Eq. (4) into

$$\nu_i + \Delta\nu_i = \frac{c}{2L}\cdot\left[N_i + \Delta N_i + \frac{2\cdot\phi(\nu_i+\Delta\nu_i)}{2\pi}\right], \tag{34}$$

and have the reflection phase term approximated to first order

$$\phi(\nu_i+\Delta\nu_i) \approx \phi(\nu_i) + 2\pi\cdot\tau_i\cdot\nu_i, \tag{35}$$

where $\tau = \mathrm{d}\phi/\mathrm{d}\omega$ is the group delay and $\omega = 2\pi\cdot\nu$ is the angular frequency. To maintain an f that is least changed, if ν_1 is changed by one FSR, i.e., $\Delta N_1 = 1$ and $\Delta\nu_1 = f_{\text{FSR}}$, due to the frequency-doubling process, ν_2 has to change by two FSR's, i.e., $\Delta N_2 = 2$ and $\Delta\nu_2 = 2\cdot f_{\text{FSR}}$. Under this condition, the change in f for $\Delta\nu_1 = f_{\text{FSR}}$ is

$$\Delta f = \frac{\Delta\nu_2}{2} - \Delta\nu_1 = 2\pi\cdot f_{\text{FSR}}^2\cdot\left[\frac{\tau_2}{2} - \tau_1\right]. \tag{36}$$

Our bichromatic cavity mirror coating is simulated to have $\tau_1 = 5.97$ fs and $\tau_2 = 6.70$ fs. Plugging these numbers into Eq. (36), we have $\Delta f \approx -0.8$ kHz. In other words, when ν_1 is changed by one FSR (≈ 552.1 MHz) in our setup, f changes by around -0.8 kHz.

Such dependence on absolute optical frequencies is derived in hindsight with respect to our measurement data. We estimate the optical frequencies of the NPRO lasers to fall in a total range of about $\pm 5\cdot f_{\text{FSR}}$ on the basis of the typical temperature tuning coefficient of the NPRO laser (≈ -3 GHz/K) in conjunction with the temperature range used in our measurements. The corresponding uncertainty in the measurement of f^+ and f^- is around ± 4 kHz, which in combination with the rmse of the linear fit of the f_{FSR} measurement in Fig. 7 still falls short of the rmse of the linear fits of the f^+ and f^- measurements.

It is therefore plausible to argue that there might be additional systematic errors in our measurements that are common mode to f^+, f^- and cancel out in f_{FSR}.

6. CONCLUSIONS

We have constructed a bichromatic optical setup to measure the temperature dependence of the difference in the coating reflection phase between two quasi-harmonic wavelengths. Our measurement result confirms our coating design approach, and the Monte Carlo simulations that take into account coating manufacturer errors [27]. The constrained temperature dependence is essential for the success of the surrogate control scheme anticipated for high-finesse cavity applications such as the dual-cavity enhance light-shining-through-a-wall experiments searching for axion-like particles. One other notable application, as mentioned in the introduction, is the control of the detuned optical cavity used to provide the frequency-dependent rotation of the squeeze angle of the squeezed vacuum state.

To better explain the experiment data, we have developed an extended model. The expected frequency differences, i.e., f^+ and f^-, calculated from the extended model agree well with the experiment data. The slight discrepancy is analyzed to most likely arise from the difference in cavity length sensed by the two quasi-harmonic fields. The extended model also shed light on the elevated rmse of the measurements of f^+ and f^- in comparison to those of f_{FSR}, but does not provide a full account.

The main results of our experiment match well our models on the bichromatic cavity and its constituent dielectric coatings. The developed model can be applied to the generalized design of surrogate cavity control schemes for optimal performance.

Disclosures. The authors declare no conflicts of interest.

Data availability. Data underlying the results presented in this paper are not publicly available at this time but may be obtained from the authors upon reasonable request.

REFERENCES

1. B. J. Meers, "Recycling in laser-interferometric gravitational-wave detectors," Phys. Rev. D **38**, 2317–2326 (1988).
2. A. Rüdiger, R. Schilling, L. Schnupp, *et al.*, "A mode selector to suppress fluctuations in laser beam geometry," Opt. Acta **28**, 641–658 (1981).
3. B. Willke, N. Uehara, E. K. Gustafson, *et al.*, "Spatial and temporal filtering of a 10-W Nd:YAG laser with a Fabry–Perot ring-cavity premode cleaner," Opt. Lett. **23**, 1704–1706 (1998).

4. R. W. P. Drever, J. L. Hall, F. V. Kowalski, *et al.*, "Laser phase and frequency stabilization using an optical resonator," Appl. Phys. B **31**, 97–105 (1983).
5. E. D. Black, "An introduction to Pound–Drever–Hall laser frequency stabilization," Am. J. Phys. **69**, 79–87 (2001).
6. T. Hansch and B. Couillaud, "Laser frequency stabilization by polarization spectroscopy of a reflecting reference cavity," Opt. Commun. **35**, 441–444 (1980).
7. D. A. Shaddock, M. B. Gray, and D. E. McClelland, "Frequency locking a laser to an optical cavity by use of spatial mode interference," Opt. Lett. **24**, 1499–1501 (1999).
8. B. P. Abbott, R. Abbott, T. D. Abbott, *et al.*, "Observation of gravitational waves from a binary black hole merger," Phys. Rev. Lett. **116**, 061102 (2016).
9. D. V. Martynov, E. D. Hall, B. P. Abbott, *et al.*, "Sensitivity of the advanced LIGO detectors at the beginning of gravitational wave astronomy," Phys. Rev. D **93**, 112004 (2016).
10. H. J. Kimble, Y. Levin, A. B. Matsko, *et al.*, "Conversion of conventional gravitational-wave interferometers into quantum nondemolition interferometers by modifying their input and/or output optics," Phys. Rev. D **65**, 022002 (2001).
11. R. Schnabel, "Squeezed states of light and their applications in laser interferometers," Phys. Rep. **684**, 1–51 (2017).
12. L. Barsotti, J. Harms, and R. Schnabel, "Squeezed vacuum states of light for gravitational wave detectors," Rep. Prog. Phys. **82**, 016905 (2018).
13. Y. Zhao, N. Aritomi, E. Capocasa, *et al.*, "Frequency-dependent squeezed vacuum source for broadband quantum noise reduction in advanced gravitational-wave detectors," Phys. Rev. Lett. **124**, 171101 (2020).
14. L. McCuller, C. Whittle, D. Ganapathy, *et al.*, "Frequency-dependent squeezing for advanced LIGO," Phys. Rev. Lett. **124**, 171102 (2020).
15. F. Acernese, M. Agathos, A. Ain, *et al.*, "Frequency-dependent squeezed vacuum source for the advanced Virgo gravitational-wave detector," Phys. Rev. Lett. **131**, 041403 (2023).
16. F. Hoogeveen and T. Ziegenhagen, "Production and detection of light bosons using optical resonators," Nucl. Phys. B **358**, 3–26 (1991).
17. P. Sikivie, D. B. Tanner, and K. van Bibber, "Resonantly enhanced axion-photon regeneration," Phys. Rev. Lett. **98**, 172002 (2007).
18. G. Mueller, P. Sikivie, D. B. Tanner, *et al.*, "Detailed design of a resonantly enhanced axion-photon regeneration experiment," Phys. Rev. D **80**, 072004 (2009).
19. P. W. Graham, I. G. Irastorza, S. K. Lamoreaux, *et al.*, "Experimental searches for the axion and axion-like particles," Annu. Rev. Nucl. Part. Sci. **65**, 485–514 (2015).
20. F. Chadha-Day, J. Ellis, and D. J. E. Marsh, "Axion dark matter: what is it and why now?" Sci. Adv. **8**, eabj3618 (2022).
21. Y. K. Semertzidis and S. Youn, "Axion dark matter: how to see it?" Sci. Adv. **8**, eabm9928 (2022).
22. D. F. J. Kimball and K. van Bibber, eds., *The Search for Ultralight Bosonic Dark Matter* (Springer, 2022).
23. L.-W. Wei, K. Karan, and B. Willke, "Optics mounting and alignment for the central optical bench of the dual cavity enhanced light-shining-through-a-wall experiment ALPS II," Appl. Opt. **59**, 8839–8847 (2020).
24. R. Bähre, B. Döbrich, J. Dreyling-Eschweiler, *et al.*, "Any light particle search II — Technical Design Report," J. Instrum. **8**, T09001 (2013).
25. R. Shah, K.-S. Isleif, F. Januschek, *et al.*, "TES detector for ALPS II," in *Proceedings of The European Physical Society Conference on High Energy Physics — PoS(EPS-HEP2021)* (2022), p. 801.
26. J. A. R. Gimeno, K.-S. Isleif, F. Januschek, *et al.*, "The TES detector of the ALPS II experiment," Nucl. Instrum. Methods Phys. Res. Sect. A **1046**, 167588 (2023).
27. L.-W. Wei, H. Hollis, A. D. Spector, *et al.*, "Temperature dependence optimized dielectric mirror coating designs for quasi-harmonic cavity resonance," (in preparation).
28. M. D. Ortiz, J. Gleason, H. Grote, *et al.*, "Design of the ALPS II optical system," Phys. Dark Universe **35**, 100968 (2022).
29. T. J. Kane and R. L. Byer, "Monolithic, unidirectional single-mode Nd:YAG ring laser," Opt. Lett. **10**, 65–67 (1985).
30. P. Hidnert and H. S. Krider, "Thermal expansion of aluminum and some aluminum alloys," J. Res. Natl. Bur. Stand. **48**, 209–220 (1952).
31. Y. Zhao, E. Capocasa, M. Eisenmann, *et al.*, "Improving the stability of frequency-dependent squeezing with bichromatic control of filter cavity length, alignment, and incident beam pointing," Phys. Rev. D **105**, 082003 (2022).